

Hierarchical porous NiCo_2O_4 nanomaterials with excellent cycling behavior for electrochemical capacitors via a hard-templating route

Rui Ding · Li Qi · Mingjun Jia · Hongyu Wang

Received: 16 July 2012 / Accepted: 8 October 2012 / Published online: 20 October 2012
© Springer Science+Business Media Dordrecht 2012

Abstract Hierarchical porous nickel cobaltite (NiCo_2O_4) nanomaterials were synthesized via a hard-templating route. The obtained materials consist of nanostructured cubic NiCo_2O_4 spinels and a spot of cubic NiO nanoparticles, and the materials display a typical hierarchical porous structure. The NiCo_2O_4 electrode displays quasi-reversible dynamics characteristics, mainly Faradaic capacitance behavior and capacitance relaxation feature. The NiCo_2O_4 electrode exhibits an excellent long cycling behavior with no capacitance decays during 5,000 cycles at a current density of 2 A g^{-1} in 1 M KOH electrolytes, and the NiCo_2O_4 electrode exhibits both high power and energy performances even after 5,000 cycles with respective value of $1,758 \text{ W kg}^{-1}$ and 8.3 W h kg^{-1} in 1 M KOH electrolytes, indicating that the NiCo_2O_4 nanomaterials are promising candidates for electrochemical capacitors.

Keywords Nickel cobaltite (NiCo_2O_4) · Electrochemical capacitors · Cycling behavior · Hierarchical porous · Hard-templating

1 Introduction

The consumption of traditional energy resources as well as the desire to reduce high CO_2 emissions associated with their use has led to significant interest in developing sustainable and clean energy products [1–5], such as electricity produced from wind- or solar-based technologies. As a result of the intermittent availability of these resources, the realization of their full potential will also require the development of new and advanced energy storage and delivery systems. Electrochemical capacitors (or supercapacitors), as a new class of energy storage devices, are now attracting intensive attention [2] because of their ability to store energy comparable to certain types of batteries, but with the advantage of delivering the stored energy much more rapidly than batteries [3]. This property makes electrochemical capacitors ideal to augment traditional batteries in many different applications. However, to become primary devices for power supply, electrochemical capacitors must be developed further to improve their abilities of energy density, power density, and especially long cycling life [6].

For an electrochemical capacitor, the superiority of electrode materials is crucial for the clean, efficient, and versatile use of energy. RuO_2 is a well-known electrode material with a high electrochemical reversibility and a high specific capacitance of over 700 F g^{-1} [7, 8]. However, RuO_2 is very expensive and toxic. Thus far, various kinds inexpensive transition metal oxides as electrode materials have been put forward for electrochemical capacitors, primarily including binary compounds of MnO_2 [9, 10], NiO [11, 12], Co_3O_4 [13, 14], etc.

However, few research works concern on the preparation of ternary compounds toward electrochemical capacitors in the literatures. It has been reported that spinel

R. Ding · L. Qi · H. Wang (✉)
State Key Laboratory of Electroanalytical Chemistry,
Changchun Institute of Applied Chemistry, Chinese Academy
of Sciences, 5625 Renmin Street, Changchun 130022, China
e-mail: hongyuwang@ciac.jl.cn

R. Ding
Graduate School of Chinese Academy of Sciences,
Beijing 100039, China

R. Ding · M. Jia
State Key Laboratory of Theoretical and Computational
Chemistry, College of Chemistry, Jilin University,
Changchun 130023, China

nickel cobaltite (NiCo_2O_4) is a very promising electrode material since it offers many intriguing advantages of low-cost, abundant resources, and environmentally friendly [15, 16]. More significantly, it is considered that NiCo_2O_4 possesses richer redox chemistry, much better electronic conductivity, and higher electrochemical activity than nickel oxides and cobalt oxides [16]. These attractive features are of huge benefit for the development of high-performance electrochemical capacitors.

Not long ago, Lu and coworkers [16] reported the novel epoxide-driven sol–gel process to prepare NiCo_2O_4 aerogels, exhibiting ultrahigh specific capacitances of $1,400 \text{ F g}^{-1}$. However, as much as we know, NiCo_2O_4 materials have still less drawn attention as electrode materials for electrochemical capacitors so far. A few current correlative papers can be indexed up to date [17–22]. Therefore, it is significant and challenging to exploit NiCo_2O_4 electrode materials for electrochemical capacitors.

Porous inorganic materials have attracted considerable interests and made a great impact in many applications, including energy storage, catalysis, and separation [23–28]. Many efforts have been devoted to the synthesis, characterizations, and applications of uniform mesoporous materials over the last decade, due to their attractive textural and structural features, e.g., highly ordered structures, ultrahigh surface area and narrow pore size distributions (PSD) in the mesopore range, tuneable pore size, and pore structure [23–27]. Progress has been made in structural, compositional, and morphological control of mesoporous materials for their emerging applications [23–27]. However, practical applications require porous materials having pore structures at different size scales to achieve better performance [23, 28]. Inclusion of macropores, mesopores, and micropores in materials combines benefits from pores in different dimensional regimes. Hierarchical porous materials, which contain interconnected macro/meso/micropores, have enhanced performance for catalysis, separation, and energy storage due to the increased mass transport through macropores and mesopores and the maintenance of a specific surface area on the level of micropore systems [23, 28].

One of the most well-known strategies for fabricating mesoporous materials is the nanocasting method using mesostructured silicas with various pore geometries (MCM-41, SBA-15, KIT-6, etc.) as “hard” templates to render negative replicas of non-siliceous materials [29–31]. However, the mesopores via a hard template is designed usually in periodic, and hierarchical pores have less been studied through this method. Herein we successfully synthesized hierarchical porous NiCo_2O_4 nanomaterials from SBA-15 (space group $P6mm$) silica templates by controlling the calcination temperature of precursors, which is similar to the method mentioned by Pellicer and coworkers [32]. The physical structures and electrochemical

performances of the as-synthesized materials were characterized and investigated, respectively. The results show that the synthesized NiCo_2O_4 materials display a typical hierarchical porous structure. The NiCo_2O_4 electrode exhibits excellent long cycling behavior and high performances even after long-term cycles, indicating a promising application in electrochemical capacitors.

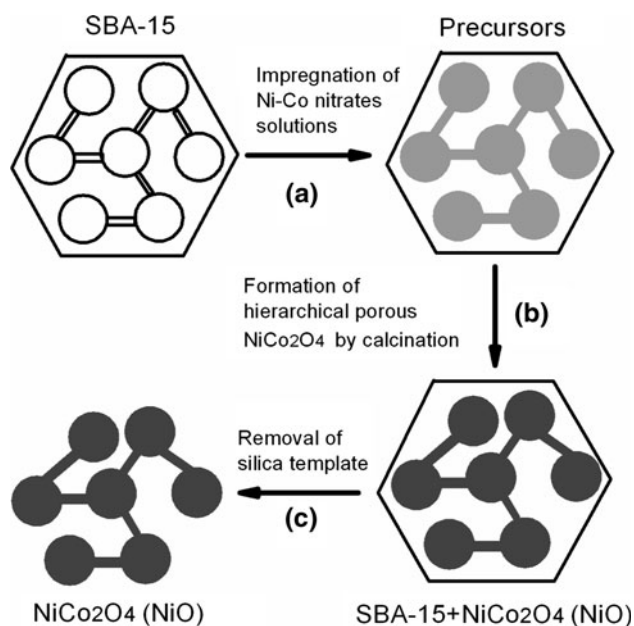
2 Experimental

2.1 Synthesis of materials

All chemicals used in this study are of analytical grade and used without further purification. In a typical procedure, SBA-15 mesoporous silica template (1.0000 g) impregnated with $\text{Co}(\text{NO}_3)_2 \cdot 6\text{H}_2\text{O}$ (0.6667 g) and $\text{Ni}(\text{NO}_3)_2 \cdot 6\text{H}_2\text{O}$ (0.3333 g) dissolved in distilled water (20 mL) under vacuum conditions with continuous magnetic stirring at room temperature for 6 h. Then, the mixture was heated at 120°C for 12 h in a box oven to evaporate solvent and cooled naturally to room temperature, afterward ground thoroughly using a mechanical grinder, and then calcined at 500°C for 5 h in a muffle stove under air atmosphere at a heating rate of 1°C min^{-1} to decompose the inorganic precursors. Subsequently, the silica matrix was removed with 2 M NaOH solution at 40°C for 24 h under magnetic stirring. Finally, the product was collected by centrifugal filtration, washed with distilled water and absolute ethanol three times in turn, and next dried at 60°C for 12 h under vacuum conditions. The formation process for the material synthesis is illustrated in Scheme 1.

2.2 Structural characterizations

Thermogravimetric analysis (TGA) and differential scanning calorimetry (DSC) were carried out with an STA 449 F3 Jupiter thermogravimetric analyzer (NETZSCH) in the temperature range from 40 to 810°C in air at a heating rate of $10^\circ\text{C min}^{-1}$. X-ray diffraction (XRD) patterns were recorded on a Rigaku-Dmax 2500 diffractometer equipped with graphite monochromatized Cu $K\alpha$ radiation source ($\lambda = 1.5406 \text{ \AA}$) at a scanning speed of 4°C min^{-1} in the range from 1° to 80° . Scanning electron microscopy (SEM) images and energy-dispersive X-ray spectrum (EDS) were conducted using Philips XL 30 and a JEOL JSM-6700F microscope. X-ray photoelectron spectra (XPS) were measured using an ESCALAB-MKII spectrometer (UK) with Al $K\alpha$ radiation (1486.6 eV) as the X-ray source for excitation, the raw spectra were curve-fitted by non-linear least squares fittings with a Gauss–Lorentz ratio (60:40) using the XPS peak fit software, and the binding energies (BEs) were evaluated using C_{1s} spectrum ($\text{BE} = 284.6 \text{ eV}$)



Scheme 1 Schematic illustration for the synthesis of hierarchical porous NiCo_2O_4 nanomaterials

as reference with the accuracy of ± 0.1 eV. Surface area and porosity were determined by nitrogen absorption at 77 K using a Micromeritics ASAP 2020 Analyzer; prior to analysis, all samples were degassed under vacuum at 120 °C for 44 h. The specific surface area was calculated using the Brunauer–Emmett–Teller (BET) method, while the PSD, average pore diameter, and pore volume were calculated from the desorption branches based on the Barrett–Joyner–Halenda (BJH) equation using Quantachrome NOVA 4000e surface analyzer.

2.3 Fabrication of working electrodes (WE)

The WE were fabricated first by pressing the homogenized mixture of 66.7 wt% active materials (the as-synthesized NiCo_2O_4 materials), 33.3 wt% conductive agent and binder (teflonized acetylene black, with an AB and PTFE mass ratio of 2:1) on each current collector (stainless steel mesh, 1 cm^2 area), and followed by drying in an vacuum oven at 80 °C for 12 h. The loading of active materials in the electrode is 6 mg cm^{-2} .

2.4 Electrochemical performances tests and evaluation

The electrochemical performances of NiCo_2O_4 electrodes were examined using a cyclic voltammetry (CV) measurement by CHI700D electrochemical workstation, a galvanostatic charging–discharging or chronopotentiometry (CP) test via Land cell tester, and an electrochemical impedance spectra (EIS) experiment through Par Sta. 2273 electrochemical instrument. Tests for the NiCo_2O_4

electrodes were carried out in a conventional three-electrode electrochemical setup which comprises an NiCo_2O_4 WE, a platinum plate counter electrode (CE), and a Hg/HgO (1 M KOH, aqueous) reference electrode (RE). CV tests were cycled between the voltage of 0 and 0.6 V with scan rates ranged from 2 to 50 mV s^{-1} , CP measurements were cycled between the voltage of 0 and 0.6 V with current densities varied from 0.5 to 6 A g^{-1} . EIS experiments were taken under a constant direct current (dc) bias potential of open circuit voltage (OCV) with an alternating current (ac) amplitude of 5 mV over the sinusoidal alternating voltage frequency range from 0.05 to 10^5 Hz. Cycle life test was conducted via a CP test between the voltage of 0 and 0.55 V at a current density of 2 A g^{-1} for 5,000 cycles. All experiments were carried out at room temperature and 1 M KOH aqueous solution was chosen as electrolyte.

The gravimetric specific capacitance (C_m , F g^{-1}), energy density (E_m , W h kg^{-1}), power density (P_m , W kg^{-1}), and coulombic efficiency (η , %), all values measured from the CP curves, were calculated according to Eqs. (1)–(4):

$$C_m = \frac{i\Delta t_d}{\Delta V} \quad (1)$$

$$E_m = \frac{1}{2} C_m (\Delta V)^2 \quad (2)$$

$$P_m = \frac{E_m}{\Delta t_d} \quad (3)$$

$$\eta = \frac{\Delta t_d}{\Delta t_c} \times 100 \quad (4)$$

where i (A g^{-1}) is current density, V (V) is the applied potential range, Δt_d and Δt_c are the time of discharging and charging branches, respectively, and m (g) is the mass of the active materials in the WE.

3 Results and discussion

3.1 Structural characteristics of NiCo_2O_4 materials

TGA–DSC measurements were carried out to investigate the thermal behavior of the Ni–Co nitrates precursors in air. As illustrated in Fig. 1, there are largely three weight loss steps in TG plots, corresponding to two times changes in the direction of heat flow in DSC curves. The first step (11.8 % weight loss) occurs in the temperature range between 40 and 158 °C with an endothermic peak in the DSC curves, corresponding to the evaporation of physical adsorbed water and the loss of part of crystal water. The second step (21.1 % weight loss) occurs in the temperature range between 158 and 420 °C with a broad exothermic peak in the DSC curves, associating with thermal

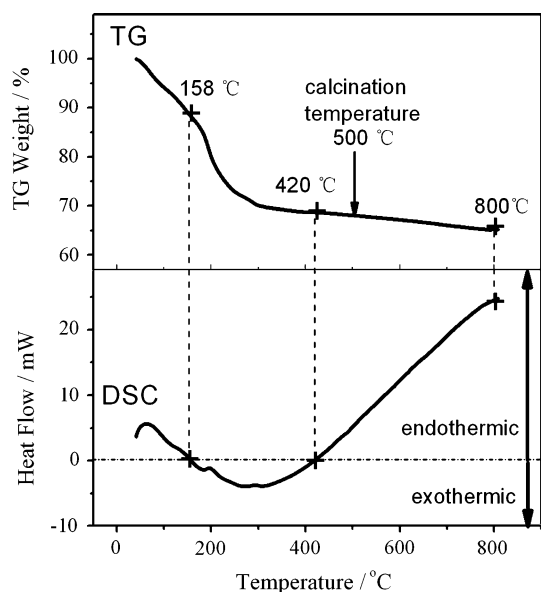


Fig. 1 TG and DSC curves of the precursors (Ni–Co nitrates)

decomposition of the Ni–Co nitrates precursors and the formation of NiCo_2O_4 spinels. The third step (3.5 % weight loss) occurs in the temperature range varying from 420 to 800 °C with a large endothermic peak in the DSC curves, owing to complete decomposition of the NiCo_2O_4 spinels [33]. On the basis of the TGA–DSC results, the temperature for calcinations of the precursors was set at 500 °C for 5 h to ensure a complete decomposition of the precursors on the one hand. On the other hand, more significantly, the calcination temperature set would contribute to the formation of a hierarchical porous structure because of some disruption and collapse of the periodic networks of ordered mesopores [32], which resulted from the partial segregation of NiO from the NiCo_2O_4 spinels (0.68 % weight loss) at more than 400 °C [34, 35]. Thus, it can be expected that the obtained NiCo_2O_4 materials are accompanied by a minor amount of NiO particles under the calcination temperature.

XRD technique is a very useful tool to determine the phase, crystallinity, and purity of materials. Figure 2 shows the typical XRD patterns of NiCo_2O_4 materials. The resultant diffraction peaks in the 2θ range from 20° to 80° basically corroborate with the standard patterns for cubic NiCo_2O_4 (JCPDS No. 73-1702) with spinel structure, but two weak shoulder peaks ($2\theta = 43.45^\circ, 63.1^\circ$) for cubic NiO (JCPDS No. 73-1579) are also detectable, indicating that the NiCo_2O_4 spinels coexist with a spot of cubic NiO phases, corresponding with the results of thermal analysis. The not obvious broad reflection at around $2\theta = 25^\circ$ related to amorphous silica corroborates the general removal of the silica template during synthesis. The largely sharp and defined diffraction lines reflect good crystalline nature of the materials, which agrees well with the SEM

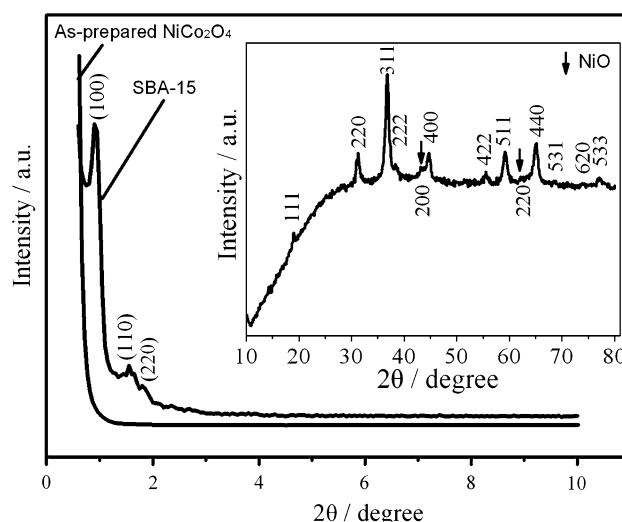


Fig. 2 XRD patterns of the NiCo_2O_4 materials

result (Fig. 3). The crystal size of the materials is calculated to be 37 nm by the Debye–Scherrer formula, i.e., Eq. (5), based on the strongest peak ($2\theta = 36.85^\circ$), which basically gets along with the SEM observations (Fig. 3). The lattice parameter a_0 of the NiCo_2O_4 spinels (space group: $Fd\bar{3}m$) determined from the observed d -spacing for crystal plane (311) at 2θ value of 36.85° using Eqs. (6) and (7) for a cubic lattice is 0.8090 nm, which lightly deviates to the standard value of 0.8110 nm for NiCo_2O_4 spinel structure (JCPDS 20-0781); beyond some errors in the determination of Bragg angles associated with the broad diffraction lines of the patterns, it may be ascribed to the formation of minor NiO phases (space group: $Fm\bar{3}m$), which is the same as the deviation phenomenon reported in the literature [36].

The low-angle XRD analysis reveals the absence of three peaks ($2\theta = 0.9^\circ, 1.55^\circ, 1.8^\circ$) for the NiCo_2O_4 materials, indicating that the NiCo_2O_4 materials are not the periodic characteristics of mesopores of the SBA-15 template but a hierarchical porous structure, which is due to some disruption and even collapse of the periodic networks of ordered pores that are induced by the partial segregation of NiO from the NiCo_2O_4 spinels, the possible incomplete filling of the silica mesochannels, the agglomeration of bulk particles outside the silica host, and pore blocking during calcinations [32], all leading to the formation of hierarchical porous structure.

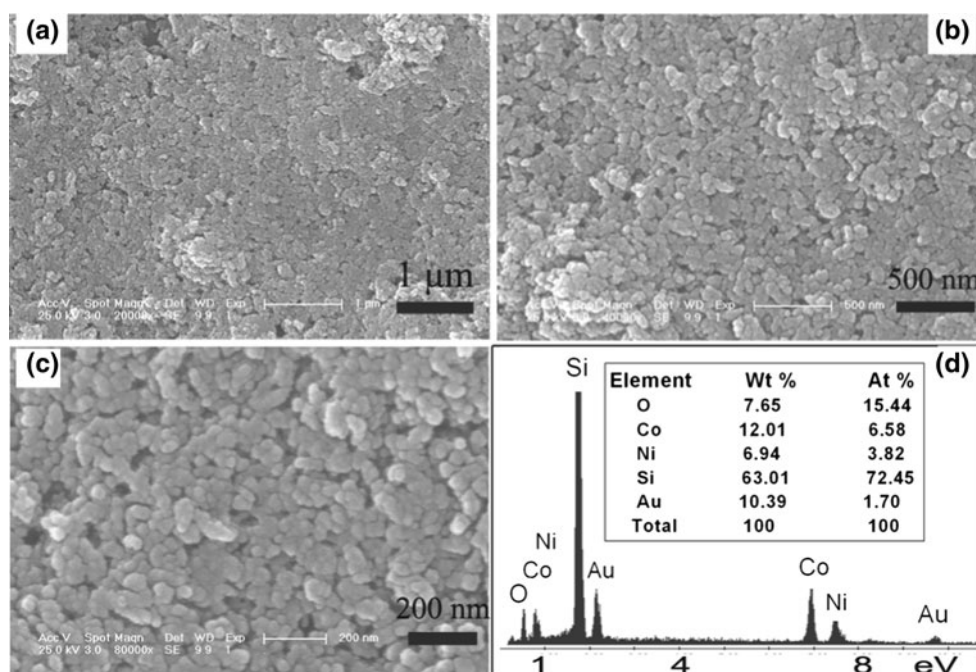
$$D = \frac{k\lambda}{(\beta \cos \theta)} \quad (5)$$

$$a_0 = d(h^2 + k^2 + l^2)^{1/2} \quad (6)$$

$$2d \sin \theta = \lambda \quad (7)$$

where D is the average crystallite size, k is Scherrer constant (0.89), λ is the wavelength of X-ray radiation (1.5406 Å),

Fig. 3 **a–c** SEM images of the NiCo_2O_4 materials at different magnifications and **d** EDS analysis of the NiCo_2O_4 materials



β is the full width at half maximum of the diffracted peak, θ is the Bragg angle of diffraction, d is observed space for crystal plane, and h, k, l are the Miller indices.

The SEM images of NiCo_2O_4 materials are shown in Fig. 3a–c. The observed NiCo_2O_4 particles have a grain-stacked structure with an average diameter of about 40 nm. Note that there exist a few large particle groups with diameter range of 0.5–1 μm which originated from the agglomeration of small-sized grains during calcinations. In addition, the materials consist of an obvious hierarchical porous structure with different (macro/meso/micro) pore sizes. Such an open hierarchical porous texture permits easy access for ions to the electrode/electrolyte interface, which is crucial for surface Faradaic reactions [37–41].

The chemical compositions of the materials were investigated by EDS, the results given in Fig. 3d show the presence of O, Co, and Ni elements with an average atomic ratio of O:Co:Ni of 4.04:1.72:1, deviating to the stoichiometric molar ratio of 4:2:1 in the NiCo_2O_4 spinel, after excluding some experimental errors, which may be explained by the formation of NiO and adsorbed water. Herein, the signals of the Si element originated from the silicon plate as support during the measurement and possible residual SiO_2 left behind in the materials, and Au was used to enhance the surface conductivity of the materials for the analysis and is also visible in the EDS patterns.

BET measurements were carried out to study the specific surface areas and the pore structure of NiCo_2O_4 materials. Typical nitrogen adsorption/desorption isotherms, and corresponding PSD and pore volume plots of

the materials are shown in Fig. 4a–c. The nitrogen sorption isotherms of the materials can be classified as type IV with H3 type hysteresis loop behavior according to the IUPAC classification, typical characteristics of mesoporous materials. The specific surface area, cumulative pore volume, and average pore diameter of the materials is 123.9 $\text{m}^2 \text{g}^{-1}$, 0.569 $\text{cm}^3 \text{g}^{-1}$, and 18.4 nm, respectively. Moreover, pore size exhibits a hierarchical distribution at micropore (center at 1.7 nm), mesopore (center at 2.2, 3.4, 5.6, 17.4 nm), and macropore (50–241 nm) (Table 1) with the majority of the pores falling in the size of 17.4 nm, indicating a typical hierarchical porous structure of the materials. The pore volumes corresponding to micropore, mesopore, and macropore are 0.00814, 0.4973, and 0.0636 $\text{cm}^3 \text{g}^{-1}$, respectively (Table 1).

Note that both highly porous structure and large surface area of electrode materials are beneficial to performance of electrochemical capacitors. The porosity determines ion transfer rate in electrode and the extent of electrode/electrolyte interfacial area [42]. Generally, there are three types of pore distributions, viz. micropore (<2 nm), mesopore (2–50 nm), and macropore (>50 nm) [43]. It is well documented that macropores can serve as “ion buffering reservoirs” and micropores can enhance the charge storage, while mesopores are capable of overcoming the primary kinetic limits of electrochemical processes [28], making the penetration of electrolytes into the whole oxide matrix facile, and further reducing the diffusion resistance [44]. Surface area is contributed to electric double layer capacitance (C_{EDL}). The C_{EDL} value of the materials estimated

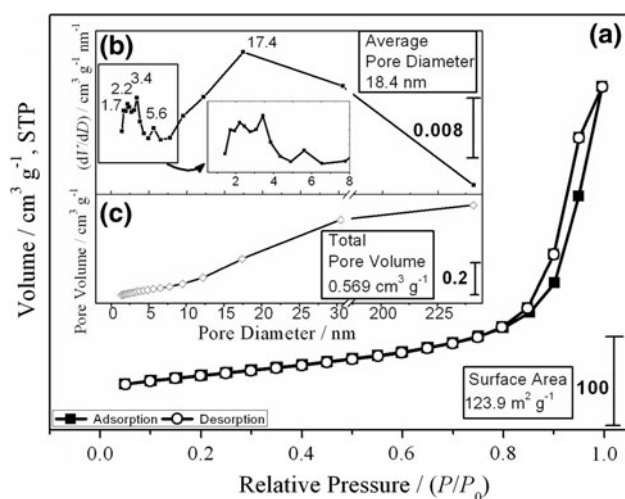


Fig. 4 BET plots of the NiCo_2O_4 materials. **a** nitrogen adsorption/desorption isotherms, **b** PSD, and **c** pore volume distribution

Table 1 BET data of the NiCo_2O_4 materials

Surface area ($\text{m}^2 \text{g}^{-1}$)	Pore size (nm) Micro-/meso-/ macro-	Pore volume ($\text{cm}^3 \text{g}^{-1}$) Micro-/meso-/ macro-
123.9	1.7/2.2, 3.4, 5.6, 17.4/50–241	0.00814/0.4973/ 0.0636

by Eq. (8) is just 24.78 F g^{-1} , implying mainly Faradaic capacitance properties of the NiCo_2O_4 materials.

$$C_{\text{EDL}} = C_{\text{STD}} \times S_{\text{BET}} \quad (8)$$

where C_{STD} represents capacitance per unit real surface area and its value equals to $20 \mu\text{F cm}^{-2}$, S_{BET} is the surface area measured by BET method.

The chemical bonding states of each element on the surface of NiCo_2O_4 materials were evaluated by XPS. Figure 5a displays the full scan spectra of the materials, which mainly contain $\text{C}_{1\text{s}}$ (as reference), $\text{O}_{1\text{s}}$, $\text{Co}_{2\text{p}}$, and $\text{Ni}_{2\text{p}}$ four core levels peaks. Of which, $\text{O}_{1\text{s}}$ spectra shown in Fig. 5b exhibit three main peaks at 533, 531.7, and 529.4 eV, associating with hydroxyl species of surface adsorbed water molecule [45, 46], oxygen ions in low coordination at the surface, and the typical of metal–oxygen bonds [47], respectively. The $\text{Co}_{2\text{p}}$ spectra shown in Fig. 5c consist of two spin–orbit doublets characteristic of Co^{2+} and Co^{3+} and two shakeup satellites (identified as “Sat.”). Similarly, the $\text{Ni}_{2\text{p}}$ spectra given in Fig. 5d are composed of two spin–orbit doublets characteristic of Ni^{2+} and Ni^{3+} and two shakeup satellites. These results show that the surface of the as-synthesized NiCo_2O_4 materials has a composition containing Co^{2+} , Co^{3+} , Ni^{2+} , and Ni^{3+} , which is in agreement with the results in the literature for NiCo_2O_4 spinels [46–48].

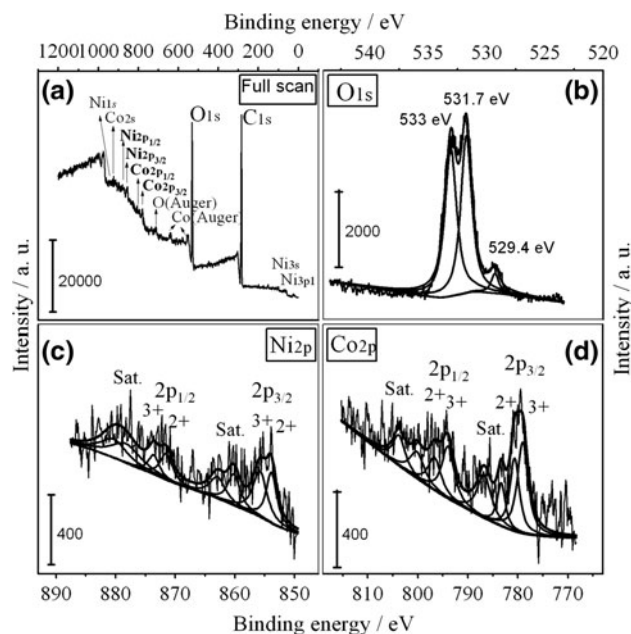


Fig. 5 XPS profiles of the NiCo_2O_4 materials. **a** full scan, **b** $\text{O}_{1\text{s}}$ core levels, **c** $\text{Ni}_{2\text{p}}$ core levels, and **d** $\text{Co}_{2\text{p}}$ core levels

3.2 Electrochemical performances of NiCo_2O_4 electrode

Long cycle life is a very important factor for the electrode materials used in electrochemical capacitors. Figure 6 shows the cycling behavior of the NiCo_2O_4 electrode at a current density of 2 A g^{-1} . As demonstrated in the figure, the overall cycling period can be largely divided into two phases, an active phase from the 1st cycle (98 F g^{-1}) to the 500th cycle (147 F g^{-1}) and a much more stable phase from the 500th cycle (147 F g^{-1}) to the 5,000th cycle (164 F g^{-1}), indicating the capacitance relaxation property of the NiCo_2O_4 electrode which needs activation for 500 cycles under examined conditions before more effective utilization of its capacitance; the phenomenon is also demonstrated by other groups [16, 49, 50]. Moreover, the capacitance exhibits a slightly ascending trend and no decays during all cycling numbers, indicating an excellent long-term cycling endurance which should relate to its unique hierarchical porous structures that are reckoned to digest the possible volume changes while cycling [16]. The coulombic efficiency of the electrode during all cycling periods maintained nearly at 100 % judging from the linear fit, showing an excellent reversibility of the NiCo_2O_4 electrode. Based on the above analysis, the NiCo_2O_4 electrode shows an excellent cycling behavior, implying a practical application for electrochemical capacitors.

EIS is a very important tool to understand electrochemical behavior of electrode materials. Figure 7 shows EIS plots of the NiCo_2O_4 electrode in fresh and after 5,000 CP cycles. The Nyquist plots (Fig. 7a) consist of a

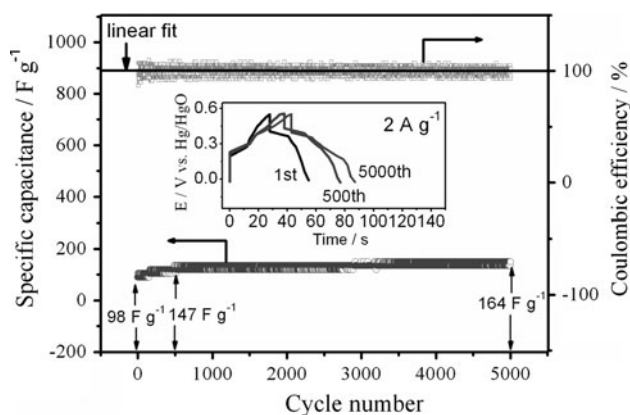


Fig. 6 Cycle life of the NiCo_2O_4 electrode at a current density of 2 A g^{-1} (Inset shows CP curves for cycles 1st, 500th and 5,000th)

semicircle in the high frequency range and a declined line deviating 90° in the low frequency area, corresponding to charge transfer resistance (R_{ct}) and the deviation to pure capacitor of the electrode, respectively. The intercept of real axis of impedance in the super-high frequency (10^5 Hz) shows the equivalent series resistance (R_{ESR} , including the resistances of electrolytes, electrode materials, and interface contacts of the electrode). The much loss of line with slope of 45° in the medium frequency region in both states suggests that Warburg resistance (Z_w) is not the determined factor in the electrode process and electrolyte ions can easily touch the electrode, reflecting high porous structure of the electrode materials, which also corresponds with the results of SEM and BET. The inset of Fig. 7a shows the charge saturation point of the electrode, the frequency response property of electrochemical capacitor, and the transition point between the high frequency and low frequency component, referred to as the “knee” or “onset” frequency (f_{knee}), which is a measure of the power capability of an electrochemical capacitor. With higher frequency, the electrochemical capacitor can be charged more rapidly or higher power density can be achieved from the electrochemical capacitor [51, 52].

The cycling stability of the NiCo_2O_4 electrode can also be examined by EIS. The results based on Fig. 7 show that the NiCo_2O_4 electrode exhibits a good cycling stability, including good capacitive behavior, electronic conductivity, electrochemical reaction rates, and power rates. The phase angles (Fig. 7b) in fresh and after 5,000 cycles at low frequency (0.05 Hz , $\Phi_{0.05\text{Hz}}$) are slightly changed (75.2° versus 70.6°), indicating that a good capacitive behavior remained after long cycles. The equivalent series resistance (R_{ESR}) (Fig. 7c) of the electrode is hardly influenced by long cycles (0.96Ω in fresh versus 1.4Ω after 5,000 cycles), indicating that a good electronic conductivity maintained after long cycles. The charge transfer resistance (R_{ct}) (Fig. 7c) of the NiCo_2O_4 electrode has increased

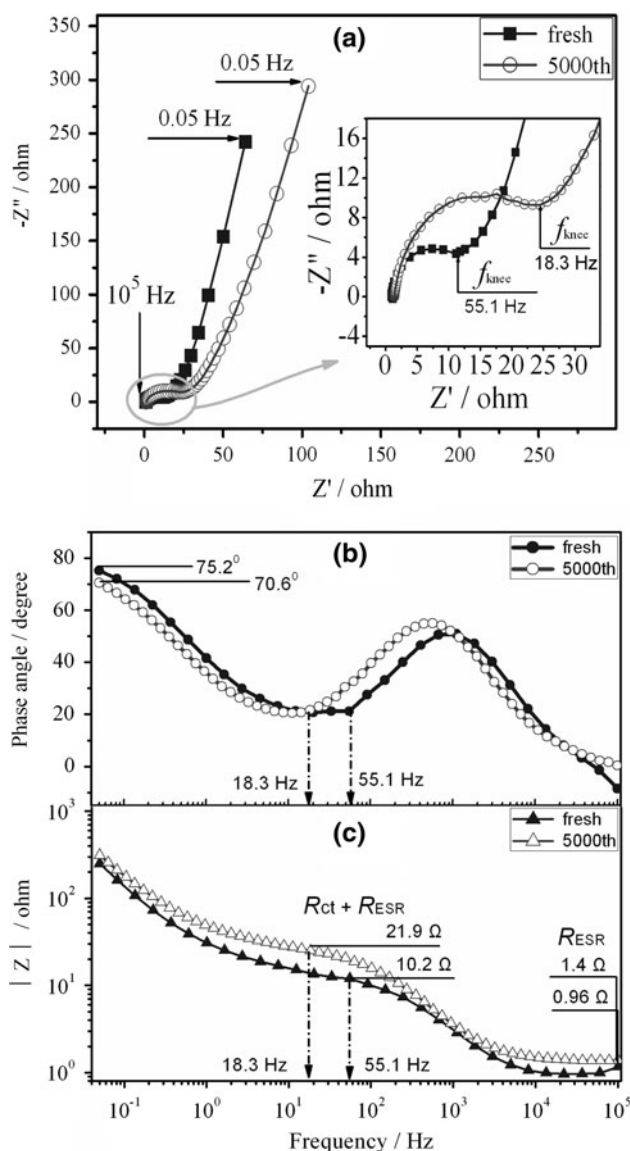


Fig. 7 EIS performances of the NiCo_2O_4 electrode in fresh and after 5,000 cycles. **a** Nyquist plots or complex plane impedance plots (Inset shows the enlarged Nyquist plots at the high frequency region), **b** Bode plots of phase angle versus frequency (in logarithmic scale), and **c** Bode plots of impedance (in logarithmic scale) versus frequency (in logarithmic scale)

11.26Ω after 5,000 cycles (20.5 versus 9.24Ω), indicating the increase of corresponding electrochemical reaction polarizations. However, considering the internal quasireversible feature of the NiCo_2O_4 electrode (see the results from following Fig. 8c–d) and the increased reactive sites (see next) after long cycles which resulted in more relaxation of electrochemical reactions and accumulative charge transfer resistance, the electrochemical reaction rates of the NiCo_2O_4 electrode after 5,000 cycles are still acceptable and comparatively stable. The reactive sites values (Z) in fresh and after 5,000 cycles are calculated to be 0.134 and 0.225 according to Eq. (9) [53]:

Fig. 8 CV performances of the NiCo_2O_4 electrode after 5,000 cycles. **a** CV plots at a scan rate of 2 mV s^{-1} , **b** CV plots at different scan rates, **c** current density of redox peaks as a function of square root of scan rates, and **d** both ratios of current density of redox peaks and potential difference of redox peaks as a function of scan rates

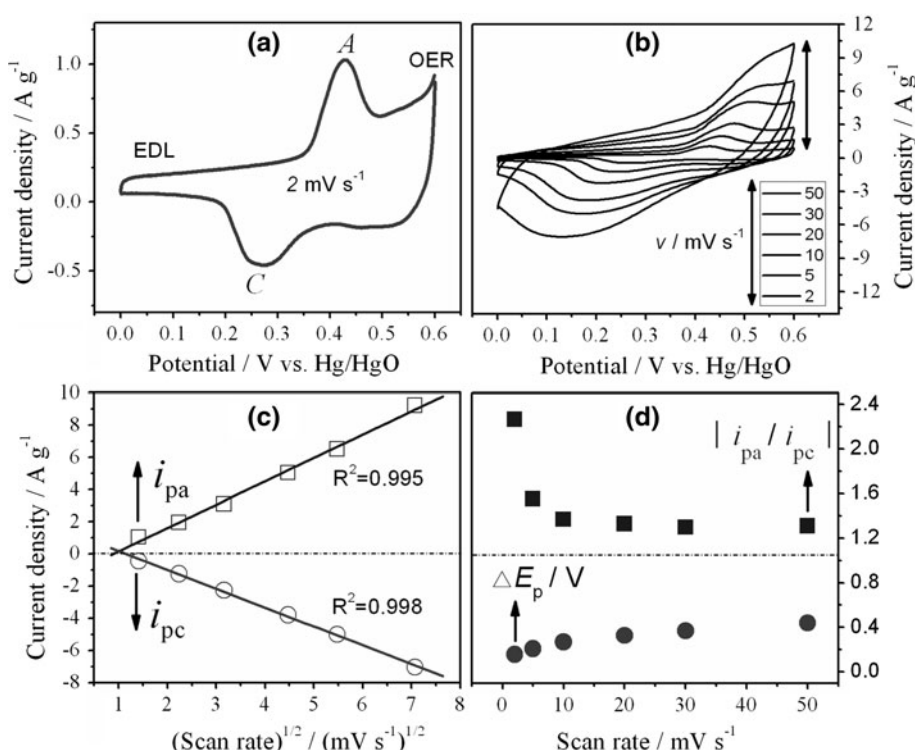


Table 2 EIS parameters of the NiCo_2O_4 electrode in fresh and after 5,000 cycles

NiCo_2O_4 electrode	$R_{\text{ESR}} (\Omega)$	$R_{\text{ct}} (\Omega)$	$\Phi_{0.05\text{Hz}} (^\circ)$	$f_{\text{knee}} (\text{Hz})$
Fresh	0.96	9.24	75.2	55.1
5,000th	1.4	20.5	70.6	18.3

$$Z = \frac{C_m M \Delta V}{F} \quad (9)$$

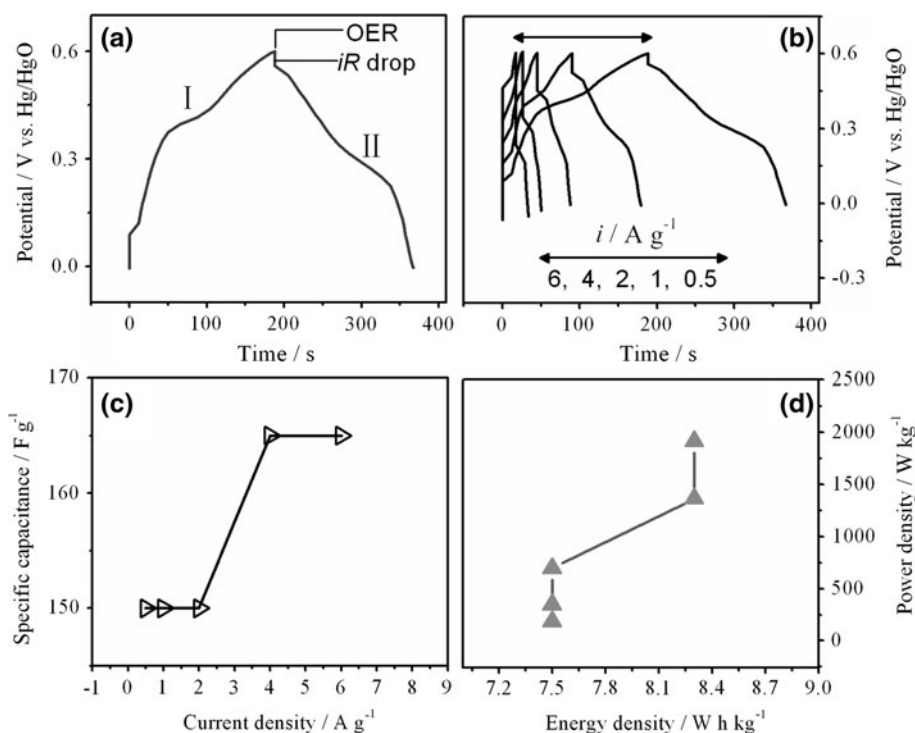
where C_m , ΔV , M , and F correspond to specific capacitance determined from charging/discharging plots (Fig. 6, the 1st and the 5,000th cycles), potential window (V), molecular weight of NiCo_2O_4 ($240.55 \text{ g mol}^{-1}$), and Faradaic constant ($96,487 \text{ C mol}^{-1}$). The knee frequencies (f_{knee}) of the NiCo_2O_4 electrode in fresh and after 5,000 CP cycles are 55.1 and 18.3 Hz, respectively, which means that the corresponding response time (i.e., reciprocal of the frequency) is about 18.1 and 54.6 ms, respectively, indicating the more relaxation feature or inferior power performance of the electrode after long cycles; however, considering the obtained much more reactive sites after long cycles that stimulate more Faradaic reactions, the power rates are still considerable and comparatively stable. The EIS parameters of the NiCo_2O_4 electrode in fresh and after 5,000 cycles are listed in Table 2.

CV performances of the NiCo_2O_4 electrode after 5,000 cycles were investigated. Figure 8a shows CV plots at a

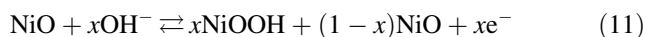
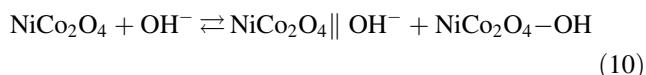
scan rate of 2 mV s^{-1} . As shown in the figure, there exist three distinct areas in the whole CV plots, an electric double layer (EDL) area (0–0.2 V), a redox reaction area (0.2–0.59 V), and an irreversible oxygen evolution reaction (OER) area (0.6 V). In EDL area, a small and approximately constant response of current density appears with the change of scanning potential, indicating that no redox reactions occur in this area, which reflects the charge storing/releasing conduct of various charged particles at the electrode/electrolyte interface, mainly the conduct of charged particles of ionic EDL. In redox reaction area, one pair of strong peak marked as (A, C) can be observed, which can be identified as redox couple $\text{Co}^{3+}/\text{Co}^{2+}$ and $\text{Ni}^{3+}/\text{Ni}^{2+}$ [54, 55] (from NiCo_2O_4), whereas the signal of redox couple $\text{Ni}^{3+}/\text{Ni}^{2+}$ (from NiO) is covered because the content of NiO is relatively low in the materials, and meanwhile its peak's position just places on the shoulder of $\text{Co}^{3+}/\text{Co}^{2+}$. In OER area, one short sharp peak corresponding to OER reaction ($4\text{OH}^- \rightarrow 2\text{H}_2\text{O} + \text{O}_2$) appears, indicating high OER electrocatalytic property of the NiCo_2O_4 materials; and the potential window of NiCo_2O_4 electrode can be no more than 0.6 V under the testing conditions lest the decomposition of electrolytes.

The capacitive property of electrode materials can also be judged from CV plots. According to the plots, the capacitance of NiCo_2O_4 electrode includes EDL capacitance (C_{EDL}) and Faradaic capacitance (C_F), which produce the respective CV curves close to an ideal rectangular shape and in the form of redox peaks. Evidently the

Fig. 9 CP performances of the NiCo_2O_4 electrode after 5,000 cycles: **a** typical CP plots at the current density of 0.5 A g^{-1} , **b** CP plots at different current densities, **c** variations of specific capacitance as a function of current density (note: all specific capacitance values were calculated by applying a full potential window of 0.6 V without deducting iR drop), and **d** Ragone plots



NiCo_2O_4 electrode mainly shows Faradaic capacitance, because the integral area of redox peaks is far more than that of rectangle. Based on the above analysis, the overall capacitance contributions of the NiCo_2O_4 electrode could be expressed as Eqs. (10) [56] and (11) [57] (considering the existence of minor NiO):



where $\text{NiCo}_2\text{O}_4\|\text{OH}^-$ represents the EDL formed by the hydroxyl ion, and $\text{NiCo}_2\text{O}_4\text{-OH}$ represents the product formed by oxidation reaction involving the hydroxyl ion.

Figure 8b shows CV plots at different scan rates. As shown in the figure, it displays nearly a center-symmetric image between anodic and cathodic processes and a fast current–potential (i – V) response at lower scan rates; however, with the increase of scan rate, anodic peaks overlapped and cathodic peaks shifted toward negative potential gradually, and i – V response happened more slowly, indicating that the NiCo_2O_4 electrode shows the quasireversible dynamics which can be further demonstrated by the results of Fig. 8c, d. Figure 8c shows a good linear relationship between the current density of redox peak and the square root of scan rate ($i_p \propto v^{1/2}$). Figure 8d shows inequality between current density of redox peaks, and an increasing trend on potential difference of redox peaks with increase of scan rates.

CP performances of the NiCo_2O_4 electrode after 5,000 cycles were also examined. Figure 9a shows CP plots at a

current density of 0.5 A g^{-1} . Essentially consistent with the CV plots of Fig. 8a, the whole CP plots can be also divided into three clear areas, i.e., an EDL linear area (0–0.2 V), a redox reaction plateau area (0.2–0.59 V) marked as (I, II), and an OER subulate peak area (0.6 V), associating with the charge storing/releasing conduct of dominant ionic EDL, the mutual conversions between redox couples $\text{Co}^{3+}/\text{Co}^{2+}$ and $\text{Ni}^{3+}/\text{Ni}^{2+}$, and the irreversible OER reactions at the electrode/electrolyte interface, respectively.

As CV, CP can also be used to determine the capacitive property of electrode materials. The CP plots in Fig. 9a show that the capacitance of NiCo_2O_4 electrode including C_{EDL} and C_F , which produces the respective CP curves with a linear and a plateau relationship between potential and time, originating from the dominant ionic EDL charging/discharging processes and the interface redox reactions, respectively. Obviously the NiCo_2O_4 electrode displays mainly Faradaic capacitance, because the charging/discharging time of plateau is far more than that of declined line.

Figure 9b exhibits CP plots at different current densities. As shown in the figure, it displays a symmetric property between charging and discharging branches and a low iR drop at lower current densities, whereas the two branches become asymmetric and the influence of iR drop becomes evident with further increase of current density, indicating quasireversible feature and unignored internal resistance of the NiCo_2O_4 electrode under high charging/discharging rates, which is in well agreement with CV performances of the electrode discussed formerly.

The C_m values with different i conditions are shown in Fig. 9c, which shows a value range from 150 to 165 F g⁻¹ when the current density changes from 0.5 to 6 A g⁻¹. Interestingly, the specific capacitance of the NiCo₂O₄ electrode shows a slightly ascending trend at much higher current densities (4 and 6 A g⁻¹). The reasons are briefly described as follows: the NiCo₂O₄ spinels are typical lattice-embedded materials that were not fully activated even by long-term cycles and the accessible reactive sites value (0.225) is very small; when charged under higher current densities, it supplies more electron transfer activation energy and makes the electrode more activated that generates more reactive sites, which contributes to more Faradaic reactions and corresponding increase of the capacitance. Here, the accessible reactive sites value (Z) of the NiCo₂O₄ electrode changes from 0.224 to 0.247 when the current density ranges from 0.5 to 6 A g⁻¹, indicating the slight increase of the reactive sites numbers under high current densities.

The Ragone plots shown in Fig. 9d summarize the performances of the electrode at various current densities. Both energy density and power density exhibit an ascending trend: the power density increases from 150.8 W kg⁻¹ (0.5 A g⁻¹) to 1,758 W kg⁻¹ (6 A g⁻¹) when energy density increases from 7.5 to 8.3 W h kg⁻¹. Based on the result, we can see that the NiCo₂O₄ electrode is capable of delivering high power and high energy simultaneously, indicating a promising application in electrochemical capacitors.

4 Conclusions

A hard-templating method was employed to synthesize hierarchical porous NiCo₂O₄ nanomaterials. The obtained materials consist of nanostructured cubic NiCo₂O₄ spinels and a minor amount of cubic NiO nanoparticles, and the materials exhibit a typical hierarchical porous structure. The NiCo₂O₄ electrode displays quasireversible characteristics of dynamics, mainly Faradaic capacitance behavior and capacitance relaxation feature. The NiCo₂O₄ electrode exhibits an excellent long cycling behavior with no capacitance decays during 5,000 cycles and the NiCo₂O₄ electrode exhibits both high power and energy performances even after 5,000 cycles (1,758 W kg⁻¹ and 8.3 W h kg⁻¹), indicating a promising application for electrochemical capacitors.

Acknowledgments We gratefully acknowledge the financial support of this research by National Basic Research Program of China (2012CB932800, 2011CB935702), Scientific Research Foundation for the Returned Overseas Chinese Scholars and State Education Ministry (SRF for ROCS, SEM) and Hundred Talents Program of Chinese Academy of Sciences.

References

1. Aricò AS, Bruce P, Scrosati B, Tarascon JM, Van Schalkwijk W (2005) *Nat Mater* 4:366
2. Liu C, Li F, Ma LP, Cheng HM (2010) *Adv Mater* 22:E28
3. Simon P, Gogotsi Y (2008) *Nat Mater* 7:845
4. Esposito DV, Hunt ST, Stottlemeyer AL, Dobson KD, Mc Candless BE, Birkmire RW, Chen JG (2010) *Angew Chem* 122:10055
5. Esposito DV, Hunt ST, Stottlemeyer AL, Dobson KD, Mc Candless BE, Birkmire RW, Chen JG (2010) *Angew Chem Int Ed* 49:9859
6. Burke A (2000) *J Power Sources* 91:37
7. Zheng JP, Cygon PJ, Jow TR (1995) *J Electrochem Soc* 142:2699
8. Zheng YZ, Ding HY, Zhang ML (2008) *Thin Solid Films* 516:7381
9. Chang JK, Lin CT, Tsai WT (2004) *Electrochem Commun* 6:666
10. Subramanian V, Zhu H, Vajtai WR (2005) *J Phys Chem B* 109:20207
11. Kuo C, Mare AA (1996) *J Electrochem Soc* 143:124
12. Yuan CZ, Gao B, Su LH, Zhang XG (2008) *Solid State Ion* 178:1859
13. Gao YY, Chen SL, Cao DX (2010) *J Power Sources* 195:1757
14. Xiong SL, Yuan CZ, Zhang XG, Xi BJ, Qian YT (2009) *Chem Eur J* 15:5320
15. Cui B, Lin H, Li JB, Li X, Yang J, Tao J (2008) *Adv Funct Mater* 18:1440
16. Wei TY, Chen CH, Chien HC, Lu SY, Hu CC (2010) *Adv Mater* 22:347
17. Salunkhe RR, Jang K, Yu H, Yu S, Ganesh T, Han SH, Ahn H (2011) *J Alloys Compds* 509:6677
18. Wu YQ, Chen XY, Ji PT, Zhou QQ (2011) *Electrochim Acta* 56:7517
19. Kandalkar SG, Lee HM, Seo SH, Lee K, Kim CK (2011) *Korean J Chem Eng* 28:1464
20. Jiang H, Ma J, Li CZ (2012) *Chem Commun* 48:4465
21. Wang HW, Hu ZA, Chang YQ, Chen YL, Wu HY, Zhang ZY, Yang YY (2011) *J Mater Chem* 21:10504
22. Wang CH, Zhang X, Zhang DC, Yao C, Ma YW (2012) *Electrochim Acta* 63:220
23. Yuan ZY, Su BL (2006) *J Mater Chem* 16:663
24. Lee J, Kim J, Hyeon T (2006) *Adv Mater* 18:2073
25. Lu AH, Schuth F (2006) *Adv Mater* 18:1793
26. Wang YQ, Yang CM, Schmidt W, Spliethoff B, Bill E, Schuth F (2005) *Adv Mater* 17:53
27. Lai XY, Li XT, Geng WC, Tu JC, Li JX, Qiu SL (2007) *Angew Chem Int Ed* 46:738
28. Wang DW, Li F, Liu M, Lu GQ, Cheng HM (2008) *Angew Chem Int Ed* 47:373
29. Tiemann M (2008) *Chem Mater* 20:961
30. Tian B, Liu X, Solovyov LA, Liu Z, Yang H, Zhang Z, Xie S, Zhang F, Tu B, Yu C, Terasaki O, Zhao D (2004) *J Am Chem Soc* 126:865
31. Wan Y, Yang H, Zhao D (2006) *Acc Chem Res* 39:423
32. Cabo M, Pellicer E, Rossinyol E, Castell O, Suriñach S, Baró MD (2009) *Cryst Growth Des* 9:4814
33. Peshev P, Toshev A, Gyurov G (1989) *Mater Res Bull* 24:33
34. Verma S, Joshi HM, Jagdale T, Chawla A, Chandra R, Ogale S (2008) *J Phys Chem C* 112:15106
35. Kobayashi Y, Ke X, Hata H, Schiffer P, Mallouk TE (2008) *Chem Mater* 20:2374
36. Chi B, Li JB, Han YS (2004) *Int J Hydrogen Energy* 29:605
37. Xing W, Li F, Yan ZF, Lu GQ (2004) *J Power Sources* 134:324
38. Wu MQ, Gao JH, Zhang SR, Chen A (2006) *J Porous Mater* 13:407

39. Zhao DD, Xu MW, Zhou WH, Zhang J, Li HL (2008) *Electrochim Acta* 53:2699
40. Zhou WJ, Zhang J, Xue T, Zhao DD, Li HL (2008) *J Mater Chem* 18:905
41. Xu MW, Bao SJ, Li HL (2007) *J Solid State Electrochem* 11:372
42. Liu Y, Zhao WW, Zhang XG (2008) *Electrochim Acta* 53:3296
43. Lastoskie C, Gubbins KE, Quirkett N (1993) *J Phys Chem* 97:4786
44. Chang KH, Hu CC, Chou CY (2007) *Chem Mater* 19:2112
45. Hashemi T, Brinkman AW (1992) *J Mater Res* 7:1278
46. Kim JG, Pugmire DL, Battaglia D, Langell MA (2000) *Appl Surf Sci* 165:70
47. Marco JF, Gancedo JR, Gracia M, Gautier JL, Rios E, Berry FJ (2000) *J Solid State Chem* 153:74
48. Thissen A, Ensling D, Fernandez Madrigal FJ, Jaegermann W, Alcantara R, Lavela P, Tirado JL (2005) *Chem Mater* 17:5202
49. Hu CC, Chang KH, Hsu TY (2008) *J Electrochem Soc* 155:F196
50. Wu YT, Hu CC (2004) *J Electrochem Soc* 151:A2060
51. Du C, Pan N (2006) *J Power Sources* 160:1487
52. Huang CW, Wu YT, Hu CC, Li YY (2007) *J Power Sources* 172:460
53. Srinivasan V, Weidner JW (2000) *J Electrochem Soc* 147:880
54. Yuan CZ, Zhang XG, Su LH, Gao B, Shen LF (2009) *J Mater Chem* 19:5772
55. Wei TY, Chen CH, Chang KH, Lu SY, Hu CC (2009) *Chem Mater* 21:3228
56. Choi D, Blomgren GE, Kumta PN (2006) *Adv Mater* 18:1178
57. Justin P, Meher SK, RangaRao G (2010) *J Phys Chem C* 114:5203